Materials Today Bio 19 (2023) 100577

Contents lists available at ScienceDirect

Materials Today Bio

journal homepage: www.journals.elsevier.com/materials-today-bio

A photodynamic-mediated glutamine metabolic intervention nanodrug for triple negative breast cancer therapy

Cancan Yu [a,1], Ningning Wang [a,1], Xiangwu Chen [a], Yue Jiang [a], Yuxia Luan [a], Wen Qin [b,**], Wenxiu He [a,*]

[a] Key Laboratory of Chemical Biology (Ministry of Education), NMPA Key Laboratory for Technology Research and Evaluation of Drug Products, School of Pharmaceutical Sciences, Cheeloo College of Medicine, Shandong University, Jinan, 250012, China
[b] Shandong University Hospital, Cheeloo College of Medicine, Shandong, University, Jinan 250012, China

ARTICLE INFO

Keywords:
Photodynamic therapy
Glutamine metabolic intervention
BPTES
Ce6
Triple negative breast cancer

ABSTRACT

"Glutamine addiction" is a unique feature of triple negative breast cancer (TNBC), which has a higher demand for glutamine and is more susceptible to glutamine depletion. Glutamine can be hydrolyzed to glutamate by glutaminase (GLS) for synthesis of glutathione (GSH), which is an important downstream of glutamine metabolic pathways in accelerating TNBC proliferation. Consequently, glutamine metabolic intervention suggests potential therapeutic effects against TNBC. However, the effects of GLS inhibitors are hindered by glutamine resistance and their own instability and insolubility. Therefore, it is of great interest to harmonize glutamine metabolic intervention for an amplified TNBC therapy. Unfortunately, such nanoplatform has not been realized. Herein, we reported a self-assembly nanoplatform (BCH NPs) with a core of the GLS inhibitor Bis-2-(5-phenylacetamido-1,3,4-thiadiazol-2-yl) ethyl sulfide (BPTES) and photosensitizer Chlorin e6 (Ce6) and a shell of human serum albumin (HSA), enabling effective harmonization of glutamine metabolic intervention for TNBC therapy. BPTES inhibited the activity of GLS to block the glutamine metabolic pathways, thereby inhibiting the production of GSH to amplify the photodynamic effect of Ce6. While Ce6 not only directly killed tumor cells by producing excessive reactive oxygen species (ROS), but also deplete GSH to destroy redox balance, thus enhancing the effects of BPTES when glutamine resistance occurred. BCH NPs effectively eradicated TNBC tumor and suppressed tumor metastasis with favorable biocompatibility. Our work provides a new insight for photodynamic-mediated glutamine metabolic intervention against TNBC.

1. Introduction

Breast cancer has been the most commonly diagnosed malignancy in 2020, ranking first in the mortality of women with cancer [1]. Noteworthy, triple negative breast cancer (TNBC), the most vicious subtype, accounts for approximately 15% of all invasive breast cancer cases [2]. TNBC is negative for estrogen receptor, progesterone receptor and HER2, and is characterized by high invasiveness, high metastatic risk and poor prognosis [3]. Due to the lack of approved target therapy, most clinically reported drugs for TNBC are cytotoxic agents, but their efficiency is often limited by chemoresistance and metastasis [4]. Therefore, it is urgently needed to develop novel therapeutic forms for improving the prognosis of TNBC. "Glutamine addiction" is a unique feature of TNBC metabolism, which relies on glutamine to support cell proliferation and metastasis [5]. Compared with other breast cancer subtypes, TNBC has higher glutamine demand and is more susceptible to glutamine depletion. Consequently, glutamine metabolic intervention suggests a potential strategy for improving the therapeutic outcomes of TNBC [6,7].

In TNBC, glutamine plays a critical role in providing energy source, promoting the synthesis of biological macromolecules, and maintaining the intracellular redox balance [8]. First, under the catalysis of glutaminase (GLS), glutamine is metabolized into glutamate, which is further catalyzed into α-ketoglutarate to feed the tricarboxylic acid cycle. Second, glutamine offers carbon and nitrogen sources for the biosynthesis of nucleotides, proteins and lipids. Third, glutamate, the metabolite of glutamine, is also a precursor of glutathione (GSH), which regulates the

* Corresponding author. Wenxiu He School of Pharmaceutical Sciences, Shandong University, 44 Wenhuaxi Road, Jinan, Shandong Province 250012, China.
** Corresponding author. Wen Qin
E-mail addresses: qinwen@sdu.edu.cn (W. Qin), hewenxiu@sdu.edu.cn (W. He).
[1] These authors contributed equally to this work.

https://doi.org/10.1016/j.mtbio.2023.100577
Received 24 September 2022; Received in revised form 30 January 2023; Accepted 7 February 2023
Available online 15 February 2023

intracellular redox homeostasis to protect tumor cells from oxidative damage [9,10]. Increasing evidence suggests that the GLS inhibitors are prospective to block the glutamine-involved metabolic pathways, thereby inhibiting the proliferation and metastasis of TNBC cells [11–13]. Bis-2-(5-phenylacetmido-1,2,4-thiadiazol-2-yl) ethyl sulfide (BPTES) is a selective allosteric inhibitor of kidney-type glutaminase, which can reverse the resistance of chemotherapeutic drugs [14–16]. Nevertheless, the efficacy of BPTES is hindered by the poor metabolic stability and low solubility. Worse yet, when the glutamine metabolic pathways are suppressed, TNBC cells can develop glucose-dependent compensatory metabolic pathways to achieve glutamine independent [17,18]. Thus, the development of highly efficient strategies for harmonization of glutamine metabolic intervention remains a great challenge.

Photodynamic therapy (PDT) is a minimally invasive treatment that utilizes photosensitizers to generate reactive oxygen species (ROS) under laser irradiation [19,20]. On the one hand, excessive ROS can directly kill cells by damaging the nucleic acids, proteins and lipids; on the other hand, ROS can deplete GSH to disrupt the intracellular redox balance [21]. These merits provide an opportunity to utilize the intrinsic features of PDT to harmonize the glutamine metabolic intervention. ROS produced by PDT can consume GSH produced by both the glutamine and glucose metabolic pathways, thus bolstering the effects of GLS inhibitors when glutamine resistance occurs. While the inhibition of GSH by GLS inhibitors can in turn ameliorate ROS resistance and amplify the efficacy of PDT. As a consequence, a multifunctional nanoplatform based on the GLS inhibitor and photosensitizer may be promising for TNBC treatment.

Herein, we designed a versatile nanoplatform (BCH NPs) based on the GLS inhibitor BPTES and photosensitizer Chlorin e6 (Ce6) for PDT-mediated glutamine metabolic intervention (Scheme 1). BPTES and Ce6 could self-assemble into nanoparticles via the hydrophobic and π-π stacking interactions, while human serum albumin (HSA) was utilized to increase their stability and biocompatibility [22–25]. The BCH NPs preferentially accumulated in tumor tissues by the enhanced penetration and retention effect. After internalized into tumor cells, BPTES blocked the glutamine metabolic pathways by inhibiting GLS activity, while Ce6 consumption of GSH enhanced the efficacy of BPTES. In addition, Ce6 not only directly killed tumor cells by producing excessive ROS, which was amplified by the inhibition of GSH by BPTES, but also consumed GSH to destroy redox balance. Our results demonstrated that the constructed BCH NPs effectively eradicated TNBC tumor and suppressed tumor metastasis with favorable biocompatibility. Our work provides a new insight for fighting against TNBC via photodynamic-mediated glutamine metabolic intervention.

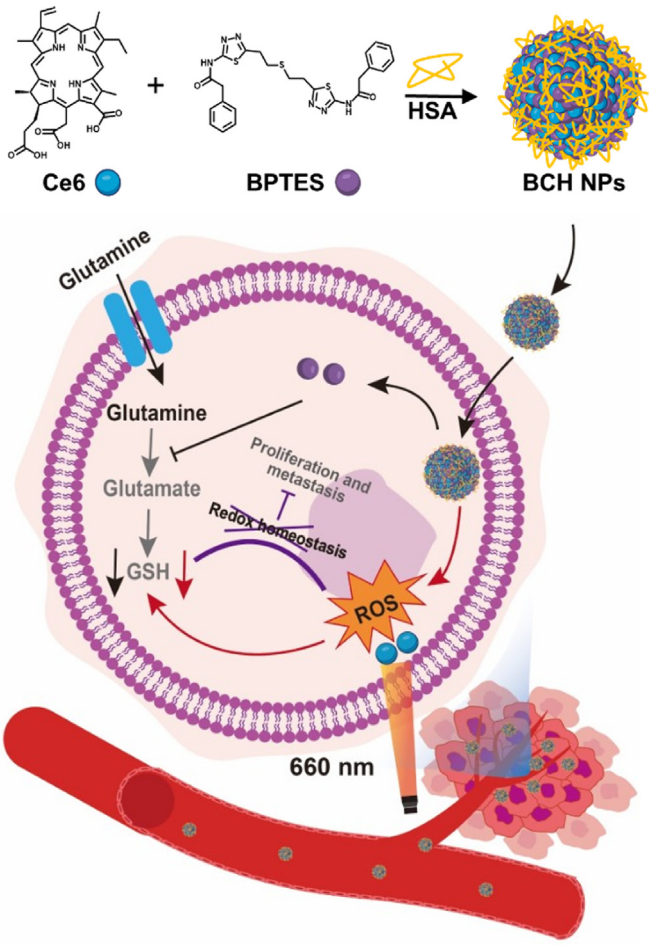

Scheme 1. Schematic illustration of the preparation of BCH nanoparticles and the photodynamic-mediated glutamine metabolic intervention mechanisms against triple negative breast cancer.

2. Materials and methods

2.1. Materials

BPTES was purchased from MedChemExpress LLC (Shanghai, China). Ce6 was purchased from J&K Scientific Ltd (Beijing, China). HSA and 2′,7′-dichlorofluorescein diacetate (DCFH-DA) were obtained from Sigma-Aldrich (USA). 1,3-diphenylisobenzofuran (DPBF) and 3-(4,5-dimethylthia-zol-2-yl)-2,5-diphenyltetrazolium bromide (MTT) were ordered from Aladdin Industrial Corporation (Shanghai, China). Hoechst 33,342 and GSH assay kit were ordered from Beijing Solarbio Science & Technology Co., Ltd (Beijing, China). Roswell Park Memorial Institute (RPMI) 1640 medium, trypsin and penicillin-streptomycin solution were obtained from Meilun biology co., Ltd (Dalian, China). Fetal bovine serum (FBS) was purchased Tianhang Biotechnology Co., Ltd (Ningbo, China).

2.2. Cells and animals

Human triple negative breast cancer cells (MDA-MB-231 cells) were cultured in a RPMI 1640 medium containing 10% FBS, and 1% penicillin-streptomycin at 37 °C with 5% CO_2. Male New Zealand White rabbits were purchased from Jinan Xilingjiao Biotechnology Co., Ltd (Jinan, China). Female BALB/CA-nu mice (4–6 weeks) were ordered from Beijing HFK Bioscience Co., Ltd (Beijing, China). All animal experiments were approved by the Animal Experimental Ethics Review Committee of Shandong University.

2.3. Preparation of BCH NPs

To prepare BCH NPs, the dimethyl sulfoxide solution containing Ce6 (1.5 mg) and BPTES (1.32 mg) was slowly dropped into 2 mL HSA solution (6 mg mL^{-1}) under stirring at 1000 rpm, then the suspension was sonicated for 30 min with an ultrasonic instrument (KQ5200DE, 200 W). Afterwards, free BPTES and Ce6 were removed by dialysis to obtain BCH NPs.

2.4. Characterization of BCH NPs

The morphology of BCH NPs was observed by a transmission electron microscopy (TEM, JEM-100CXII, JEOL, Japan). The size and zeta potential values of BCH NPs were measured by a laser particle analyzer (Zetasizer Nano ZS90, Malvern Instrument, UK). The characteristic peaks of BCH nanoparticles were characterized by an UV–vis spectrophotometer (UV–8000S, Metash, China). The entrapment efficiency and drug loading contents of Ce6 and BPTES in BCH NPs were respectively calculated by the UV–vis spectrophotometer. The chemical composition of BCH NPs was determined by scanning electron microscopy (SEM) coupled with energy-dispersive X-ray spectroscopy (EDS). To evaluate

the stability of BCH NPs in plasma, BCH NPs were incubated in PBS (pH 7.4) with 10% FBS at 4 °C for 7 days and the particle size was determined by the laser particle analyzer every 24 h.

2.5. In vitro singlet oxygen production

The *in vitro* singlet oxygen ($^1O_2$)-generating ability of BCH NPs was investigated by the probe of 1,3-diphenylisobenzofuran (DPBF), since the production of $^1O_2$ can oxidize DPBF and thus decrease its absorbance at 421 nm [26,27] Briefly, DPBF (15 μg mL^{-1}) was respectively added into water, free Ce6 (5 μg mL^{-1}), and BCH NPs (equivalent to 5 μg·mL^{-1} Ce6), and irradiated with a 660 nm laser (100 mW cm^{-2}) for different time (0, 50, 100, 150, 200, 250, 300 s). The remaining amount of DPBF was calculated using the following formula:

$$\text{Remaining DPBF } (\%) = A_t/A_0 \times 100\%$$

Where A_t represents the absorbance of each sample after receiving different irradiation time, and A_0 means the absorbance of each sample without irradiation.

2.6. Biocompatibility assay

The biocompatibility of BCH NPs was evaluated by hemolysis assay. In brief, 75 μL different concentrations of BCH NPs (from 2.5 to 50 μg mL^{-1}) were mixed with 550 μL normal saline and 625 μL 2% rabbit red blood cell suspension, the mixture was then incubated at 37 °C for 3 h. While the identical volume of normal saline and distilled water mixed with 2% red blood cell suspension were regarded as the negative control and positive control, respectively. Afterwards, each sample was centrifuged (1500 rpm) for 15 min to collect the supernatant, and the absorbance of the supernatant was detected at 540 nm. The formula for calculating hemolysis ratio was as follows:

$$\text{Hemolysis ratio } (\%) = \frac{A_{sample} - A_{negative}}{A_{positive} - A_{negative}} \times 100\%$$

Where A_{sample}, $A_{negative}$ and $A_{positive}$ represents the absorbance of BCH NPs, negative control and positive control, respectively.

2.7. Cellular uptake

To evaluate the cellular uptake of free Ce6 and BCH NPs, MDA-MB-231 cells were inoculated in 6-well plate (2 × 10^5 cells/well) and incubated for 24 h. Afterwards, the cells were incubated with fresh medium containing Ce6 or BCH NPs (equivalent to 15 μg·mL^{-1} Ce6) for 1, 2, or 4 h, respectively. The fluorescence intensity of Ce6 in each group was quantitatively determined by flow cytometer (Accuri C6 Plus, BD, USA). Besides, the cells incubated for 4 h were fixed with 4% paraformaldehyde and stained with Hoechst 33,342 for 10 min to label the nucleus for visualization under a confocal laser scanning microscope (LSM 900 with AiryScan 2, Zeiss, Germany). And the mean fluorescence intensity (MFI) in each group were calculated by Image J software.

2.8. Cytotoxicity assay

To evaluate the dark cytotoxicity of BCH NPs. MDA-MB-231 cells were seeded in 96-well plate (5 × 10^3 cells/well) and incubated for 24 h. Subsequently, 100 μL fresh medium containing BPTES, Ce6 or BCH NPs (BPTES from 1.1 to 10.7 μg mL^{-1}, Ce6 from 1 to 10 μg mL^{-1}) was added to culture the cells for 4 h. Then, the medium was discarded and updated with 100 μL drug-free medium to incubate the cells for another 20 h. To evaluate the photodynamic cytotoxicity of BCH NPs. MDA-MB-231 cells were incubated with 100 μL different concentrations of Ce6 or BCH NPs (Ce6 from 1 to 10 μg mL^{-1}) for 4 h. After that, the cells were cultured with 100 μL drug-free medium, irradiated with 660 nm laser for 5 min, and incubated for another 20 h. Cells without any treatment were regarded as the control group. Afterwards, 10 μL MTT (5 μg mL^{-1}) were added into each well and incubated for 4 h, which would be reduced by succinate dehydrogenase in the mitochondria of living cells into insoluble formazan and deposit in the cell. Then, the precipitate was dissolved with 200 μL dimethyl sulfoxide, and the absorbance of the sample was measured at 490 nm by a microplate reader (EnSight, PerkinElmer, Singapore). The cell mortality rate was calculated with the following equation:

$$\text{Cell mortality rate } (\%) = \frac{A_{\text{negative control}} - A_{sample}}{A_{\text{negative control}} - A_{blank}} \times 100\%$$

Where the $A_{\text{negative control}}$ referred to the absorbance of control group, A_{blank} was the absorbance of blank well.

2.9. Intracellular GSH consumption

The intracellular GSH consumption function of BCH NPs was determined by the GSH assay kit. In brief, MDA-MB-231 cells were seeded in 6-well plate (1 × 10^5 cells/well) and incubated overnight. Subsequently, cells were respectively incubated with fresh medium containing free Ce6, BPTES and BCH NPs (BPTES 1.05 μg mL^{-1}, Ce6 0.95 μg mL^{-1}) for 24 h. After removing the medium, the Ce6 and BCH NPs groups were irradiated with a 660 nm laser (100 mW cm^{-2}) for 5 min. Then, the cells were treated according to the protocol of the GSH assay kit and the remaining intracellular GSH was detected at 412 nm using a microplate reader.

2.10. Intracellular ROS production

The ROS production ability of BCH NPs with laser irradiation was evaluated by a DCFH-DA probe, which would be metabolized into 2′,7′-Dichlorodihydrofluorescein (DCFH), and then oxidized rapidly by the intracellular ROS into a strong fluorescent substance of 2′,7′-Dichlorofluorescein (DCF) [28,29]. In brief, MDA-MB-231 cells were seeded in 6-well plate (2 × 10^5 cells/well) and incubated for 24 h. Then, fresh medium containing Ce6 (3 μg mL^{-1}) and BCH NPs (equivalent to 3 μg·mL^{-1} Ce6) were added and incubated for 4 h. Subsequently, the cells were washed with PBS and incubated with DCFH-DA (20 μmol L^{-1}) for 20 min and irradiated with a 660 nm laser (100 mW cm^{-2}) for 5 min. Finally, the cells were harvested and the fluorescence intensity of DCF in each group was detected by flow cytometry.

2.11. In vivo distribution of BCH NPs

2 × 10^6 MDA-MB-231 cells were inoculated into the right breast pads of the female BALB/CA-nu mice. Ce6 or BCH NPs (Ce6 6 mg kg^{-1}) were respectively injected into the mice via tail vein when the tumor volume was approximately 100 mm^3. At scheduled time points (2 h, 4 h, 6 h, and 10 h post-injection), the fluorescence images of mice were observed by a *in vivo* fluorescence imaging system (IVIS Kinetic, USA).

2.12. In vivo anti-tumor and anti-metastasis effect of BCH NPs

MDA-MB-231 cells (2 × 10^6 cells/mice) were subcutaneously inoculated into the right breast pads of female BALB/CA-nu mice. When the tumor volume was about 50 mm^3, the mice were randomly divided into normal saline group (as control group), BCH NPs group, Ce6 + Laser group, BPTES + Ce6 + Laser group (as BC + Laser) and BCH NPs + Laser group. The mice were intravenously injected with normal saline, Ce6, BC, and BCH NPs (6 mg·kg^{-1} Ce6, 6.23 mg·kg^{-1} BPTES). At 2 h post-injection, the mice of Ce6 + Laser group, BC + Laser group, and BCH NPs + Laser group were irradiated with a 660 nm laser (100 mW cm^{-2}) for 5 min. All mice were treated once every two days for a total of five times. The tumor volume and body weight were monitored every two days for 30 days. The tumor volume was calculated as length × width^2/2. The mice were sacrificed 20 days after the last treatment (day 30). The

excised tumors were photographed and weighed. The apoptosis and necrosis of tumor tissues were detected by hematoxylin-eosin (H&E) staining. Besides, Lung tissues in each treatment group were excised and the number of metastatic nodules was recorded. And H&E staining of the lung tissues was observed for further metastatic study.

2.13. 13 In vivo biosafety evaluation of BCH NPs

To evaluate the biosafety of BCH NPs, the major organs (heart, liver, spleen, lung, and kidney) in each treatment group were performed with H&E staining to observe the histological changes. The serum in each treatment group were taken to detect the classic blood biochemical indexes of alanine aminotransferase (ALT), aspartate aminotransferase (AST) and creatinine (CREA) using the automatic biochemical analyzer (Chemray 240, China).

2.14. Statistical analysis

The data are displayed as mean ± standard deviation (SD). The significant difference between different groups was determined by two-way analysis of variance (ANOVA) test, ordinary one-way ANOVA test, or two-tailed Student's t-test using the GraphPad Prism 9.0 software. The level of significance: ns, no significance, $*P < 0.05$, $**P < 0.01$, $***P < 0.001$, and $****P < 0.0001$.

3. Results and discussion

3.1. Preparation and characterization of BCH NPs

BPTES and Ce6 were successfully assembled into nanoparticles with the assistance of HSA. The TEM images showed that BCH NPs were spherical morphology with uniform size (Fig. 1A). The BCH NPs displayed a mean hydration diameter of 120.8 ± 1.32 nm with a narrow distribution (polydispersity index, PDI = 0.128) and a typical Tyndall phenomenon (Fig. 1B). The BCH NPs was negatively charged and the zeta potential was −22.4 ± 1.67 mV (Fig. S1, Supporting Information). The simultaneous appearance of the characteristic UV–vis peaks of BPTES (261 nm) and Ce6 (390 nm and 660 nm) indicated that BPTES and Ce6 had been successfully assembled into BCH NPs (Fig. 1C). The entrapment efficiency of BPTES and Ce6 in BCH NPs was 92.18 ± 3.45% and 74.86 ± 1.23%, respectively. The drug loading contents of BPTES and Ce6 in BCH NPs were 11.27 ± 0.15% and 10.40 ± 0.78%, respectively. The EDS mapping results showed that the elements of carbon, oxygen, nitrogen and sulfur were uniformly distributed in BCH NPs, indicating that the components of HSA, Ce6 and BPTES were uniformly distributed in BCH NPs. (Fig. S2, Supporting Information). The particle sizes of BCH NPs did not change significantly in 10% FBS within 7 days (Fig. S3, Supporting Information), proving that BCH NPs had favorable colloidal stability in plasma. The formation of the stable nanostructure of BCH NPs was due to

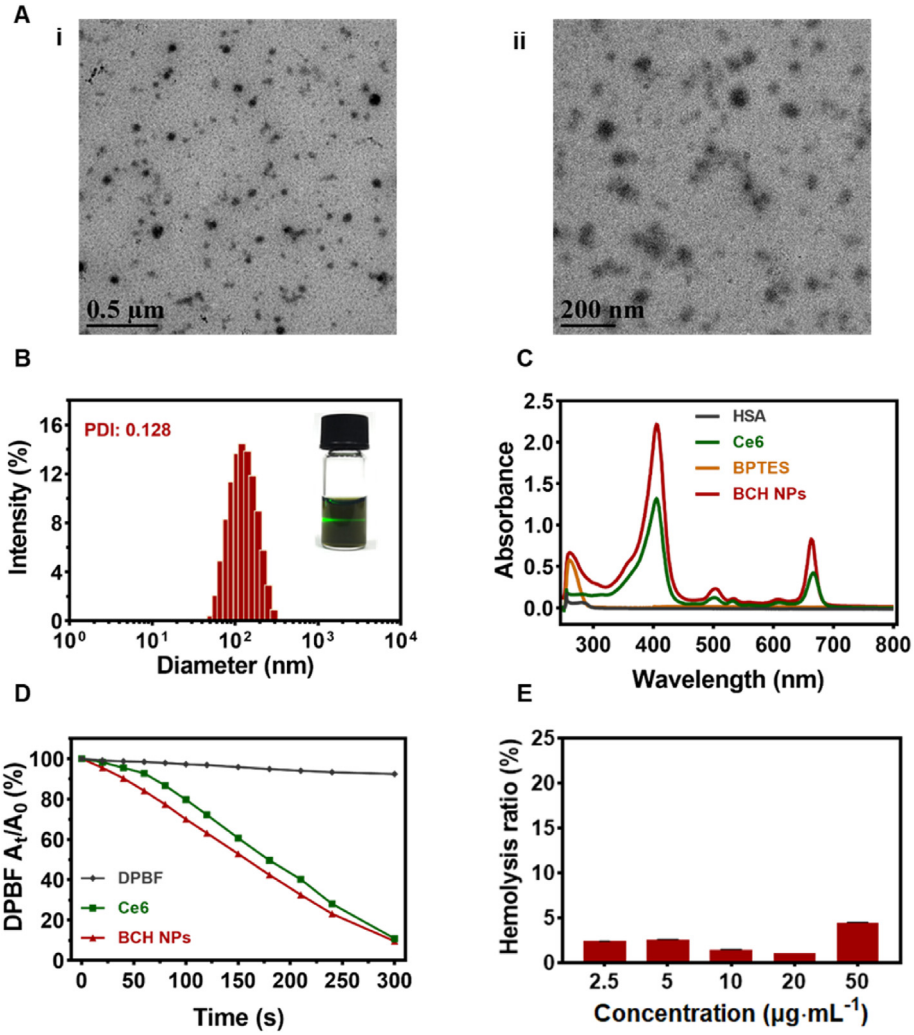

Fig. 1. (A) TEM image of BCH NPs, (i) scale bar = 0.5 μm; (ii) scale bar = 200 nm. (B) The hydrodynamic size distribution of BCH NPs, inserted was the BCH NPs solution with a typical Tyndall phenomenon. (C) The UV–vis spectra of HSA, Ce6, BPTES, and BCH NPs. (D) The $^1O_2$-generating ability of Ce6 and BCH NPs with a 660 nm laser irradiation. (E) The hemolysis ratio of different concentrations of BCH NPs (n = 3).

the strong π-π stacking and hydrophobic interaction between BPTES and Ce6, while the modification of HSA further improved the stability of BCH NPs via hydrogen bonding interaction.

The DPBF probe was used to measure the $^1O_2$-generating ability of BCH NPs. As shown in Fig. 1D, the remaining amount of DPBF in BCH NPs group was 9.56%, comparable to 10.89% in free Ce6 group. The above results indicated that loading Ce6 into BCH NPs had negligible effect on the $^1O_2$-generating ability of Ce6. In addition, although the hemolytic effect of BCH NPs was not concentration-dependent, there was no significant difference among the groups. More importantly, BCH NPs resulted in negligible hemolysis rates (all below 5%) at concentrations from 2.5 to 50 μg mL^{-1} (Fig. 1E), suggesting that HSA endowed BCH NPs with favorable biocompatibility for intravenous administration.

3.2. Cellular uptake of BCH NPs

Flow cytometry and confocal laser scanning microscope were used to investigate the cellular uptake behavior of BCH NPs. As shown in Fig. 2A (i and ii), the uptake of both Ce6 and BCH NPs was time-dependent. Fluorescent signal of Ce6 in BCH NPs group was much stronger than that in free Ce6 group at 1, 2, and 4 h, which confirmed an enhanced intracellular uptake of BCH NPs than free Ce6 (Fig. 2A iii). Similar results were also observed by the confocal laser scanning images (Fig. 2B). Quantitative results show that the mean MFI of Ce6 in BCH NPs group was 2.33-fold that of Ce6 group (Fig. S4, Supporting Information). Compared with free Ce6, the superiority of BCH NPs in cellular uptake might be that HSA can promote the efficient endocytosis of BCH NPs by binding to the secreted protein acidic and rich in cysteine overexpressed on tumor cell [30–35].

3.3. In vitro cytotoxicity, GSH consumption, and ROS production of BCH NPs

The *in vitro* cytotoxicity of BCH NPs was evaluated via MTT assay. Different concentrations of BPTES, Ce6, and BCH NPs caused less than 20% cell mortality in the absence of laser irradiation (Fig. S5, Supporting Information). On the one hand, it indicated the relatively low dark cytotoxicity and favorable biosafety of BCH NPs. On the other hand, it suggested that inhibition of glutaminase by BPTES alone without the photodynamic effect of Ce6 was not sufficient to suppress TNBC cells growth, since they could develop adaptive strategies to counteract glutamine deficiency [36–38]. By contrast, with the help of laser irradiation, both Ce6 and BCH NPs showed an enhanced cytotoxicity in a dose-dependent manner. Notably, the cytotoxicity of BCH NPs was

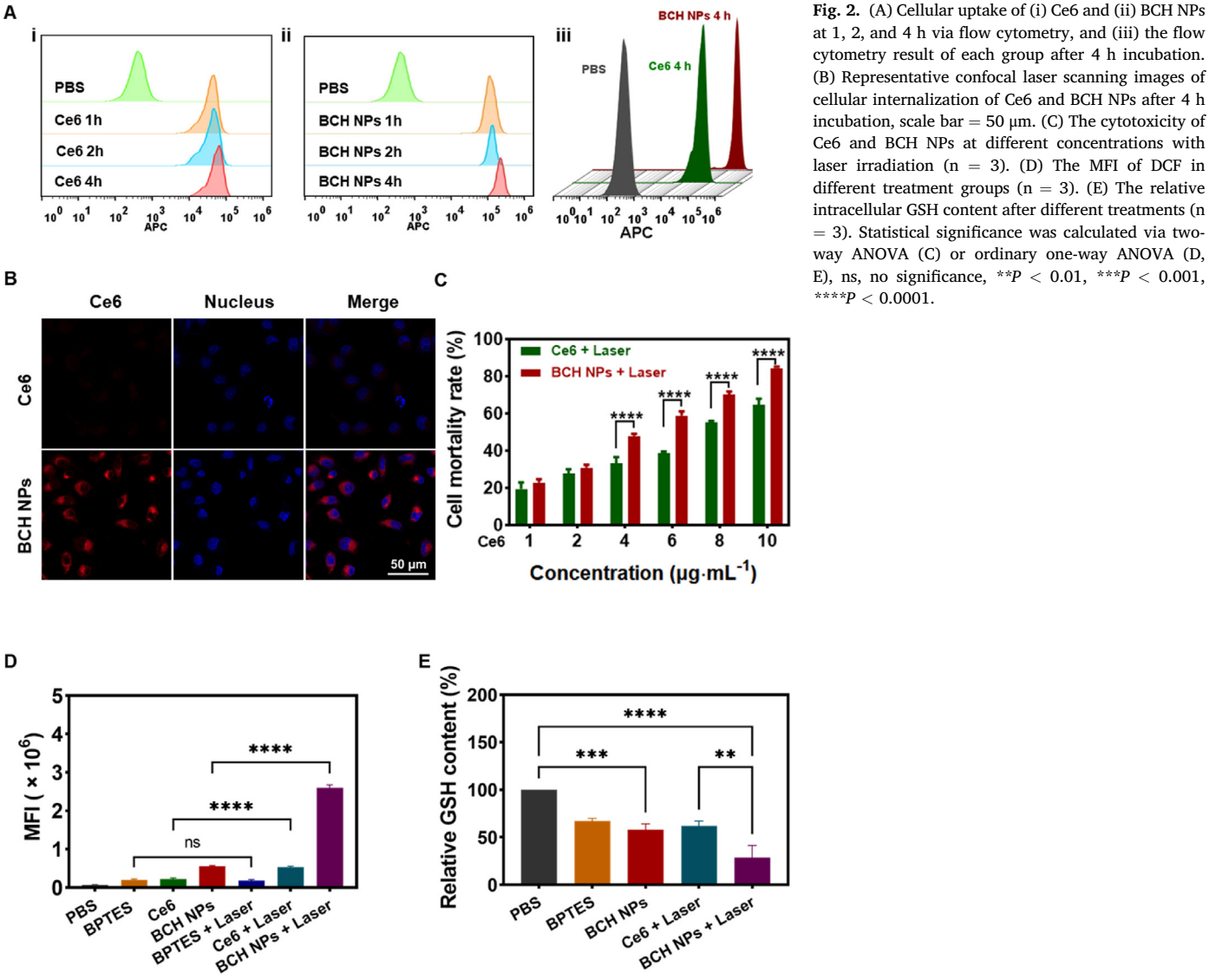

Fig. 2. (A) Cellular uptake of (i) Ce6 and (ii) BCH NPs at 1, 2, and 4 h via flow cytometry, and (iii) the flow cytometry result of each group after 4 h incubation. (B) Representative confocal laser scanning images of cellular internalization of Ce6 and BCH NPs after 4 h incubation, scale bar = 50 μm. (C) The cytotoxicity of Ce6 and BCH NPs at different concentrations with laser irradiation (n = 3). (D) The MFI of DCF in different treatment groups (n = 3). (E) The relative intracellular GSH content after different treatments (n = 3). Statistical significance was calculated via two-way ANOVA (C) or ordinary one-way ANOVA (D, E), ns, no significance, $^{**}P < 0.01$, $^{***}P < 0.001$, $^{****}P < 0.0001$.

significantly improved compared with free Ce6 (Fig. 2C). On the one hand, this was because the increased cellular uptake of BCH NPs resulted in better photodynamic effects than free Ce6; On the other hand, the synergistic effect of glutaminase inhibition by BPTES and glutathione consumption by Ce6 in BCH NPs remarkably enhanced the cytotoxicity. Taken together, photodynamic-mediated glutamine metabolic intervention by BCH NPs reflected the efficient cytotoxicity against TNBC cells.

Subsequently, the intracellular ROS production ability of BCH NPs was evaluated by the DCFH-DA probe [39]. As illustrated in Fig. 2D and Fig. S6, Supporting Information, BPTES produced negligible ROS with or without laser irradiation. By contrast, fluorescent signals of DCF in both Ce6 and BCH NPs groups increased evidently upon laser irradiation. More importantly, the MFI of DCF in the BCH NPs + Laser group was 4.85-fold that of Ce6 + Laser group, demonstrating the superior intracellular ROS production ability of BCH NPs. This was attributed to the high-efficient internalization of BCH NPs into cells via endocytosis.

BPTES inhibits the metabolism of glutamine to glutamate, thus reducing the biosynthesis of GSH, and resulting in redox dynamic imbalance [40]. Therefore, the intracellular GSH consumption of BCH NPs was detected by the GSH assay kit. As shown in Fig. 2E, compared with the control group, the relative intracellular GSH content in BPTES group decreased to 66.71 ± 2.21%, while BCH NPs without laser irradiation showed similar GSH depletion efficiency to BPTES. This was because with the extension of incubation time, the intracellular free BPTES concentration increased gradually, reaching the maximum concentration of inhibiting glutaminase [41]. Even if the concentration of BCH NPs is higher than that of BPTES, the ability of BCH NPs to inhibit GSH synthesis is similar to that of free BPTES due to the presence of glutamine resistance, which was also confirmed by the similar dark cytotoxicity results of BPTES and BCH NPs (Fig. S6, Supporting Information). By contrast, with laser irradiation, BCH NPs resulted in the least relative GSH content, accounting for only 28.76 ± 10.28% of the control group. It was because that BCH NPs could not only inhibit GSH biosynthesis by BPTES, but also consume the existing GSH through Ce6-mediated PDT, thus achieving a comprehensive GSH exhaustion. The above results proved the effectiveness of PDT-mediated glutamine metabolic intervention.

3.4. In vivo distribution of BCH NPs

To evaluate the tumor accumulation ability of BCH NPs and determine the time point of laser irradiation for the following *in vivo* antitumor assessment, we performed the *in vivo* distribution experiment on TNBC-bearing mice. As shown in Fig. 3A and B, the fluorescence intensity of Ce6 in tumor site in BCH NPs group was significantly higher than that in free Ce6 group at each time point, reflecting the preferential accumulation of BCH NPs at the tumor sites. Since BCH NPs could not only prolong the circulation time of Ce6, but also enhance the accumulation of Ce6 at the tumor sites through the enhanced permeability and retention effect [42]. In addition, the fluorescence intensity of Ce6 at the tumor sites reached the maximum at 2 h post-injection in both free Ce6 and BCH NPs groups. Therefore, laser irradiation was performed at 2 h after intravenous injection to ensure the best therapeutic efficacy.

3.5. In vivo anti-tumor growth and metastasis assessment

The *in vivo* antitumor effect of BCH NPs was evaluated by recording the tumor growth and metastasis. Compared with the control group, BCH NPs, Ce6 + Laser, BC + Laser, and BCH + Laser can suppress tumor growth to varying degrees. Due to the poor solubility and low bioavailability of BPTES, BC + Laser group failed to show better anti-tumor effect than Ce6 + Laser group, while the tumor growth was the slowest in BCH NPs + Laser group. During the following 20 days after treatment termination, tumor volume in the BCH NPs, Ce6 + Laser, and BC + Laser groups continued to increase, whereas there was little change in the BCH + Laser group (Fig. 4A–C). In the BCH NPs + Laser group, the mean tumor weight was only 0.04 ± 0.02 g, significantly lower than that of 0.59 ± 0.10 g in the control group and 0.20 ± 0.04 g in the BC + Laser group (Fig. 4D). Besides, the tumor inhibition rate of the BCH NPs + Laser group was 92.87 ± 3.94%, which was much higher than that of 77.37 ± 12.04% in BC + Laser group (Fig. 4E). Apoptotic and necrotic cells have reduced cell volume and shrunken nucleus, which can be seen as loose cell arrangement in H&E staining images [43]. The H&E staining of tumor tissues showed a large number of apoptotic and necrosis cells in the BCH NPs + Laser group (Fig. 4F).

Metastasis is the leading cause of death for TBNC patients. Therefore, we analyzed the pulmonary metastasis of TBNC tumors to further evaluate the anti-metastasis ability of BCH NPs (Fig. 5A). Notably, the average number of pulmonary metastatic nodules per lung was 17 ± 3.12 in the control group. Compared with the control group, pulmonary metastatic nodules in other treatment groups were significantly reduced. It was worth noting that the average number of metastatic nodules per lung was reduced to 0.88 ± 1.17 in the BCH NPs + Laser group, which was only 5.17% of the control group and 12.39% of the BC + Laser group (Fig. 5B and C). Furthermore, H&E staining was used to observe the metastatic regions of the lung tissues, which was characterized by a population of cells with dark stained nuclei. The metastatic regions were obviously observed in the control group, but hardly detected in the BCH + Laser group (Fig. 5D), which was consistent with the quantified results. These results suggested that the photodynamic-mediated glutamine metabolic intervention by BCH NPs successfully suppressed the pulmonary metastasis of TNBC.

Taken together, these results clearly demonstrated that BCH NPs + Laser could effectively inhibit the growth and metastasis of TNBC, which

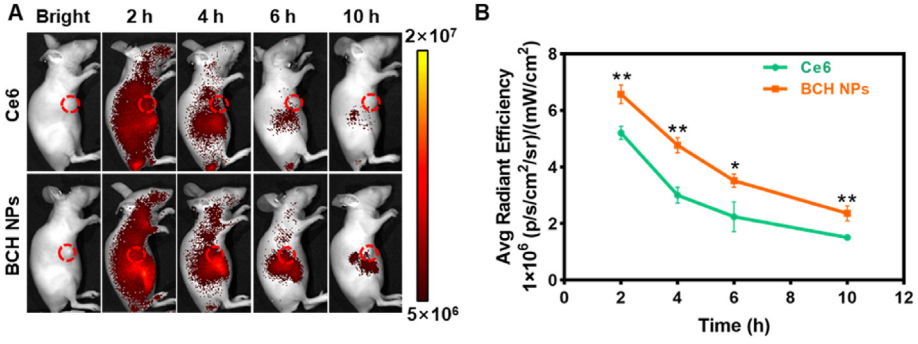

Fig. 3. (A) Representative *in vivo* fluorescence images of tumor-bearing mice injected with Ce6 or BCH NPs at different time points, the red curves represent the tumor regions. (B) Average fluorescence intensity of Ce6 in Ce6 and BCH NPs groups at different time points (n = 3). Statistical significance was calculated via two-tailed Student's t-test, $^{*}P < 0.05$, $^{**}P < 0.01$.

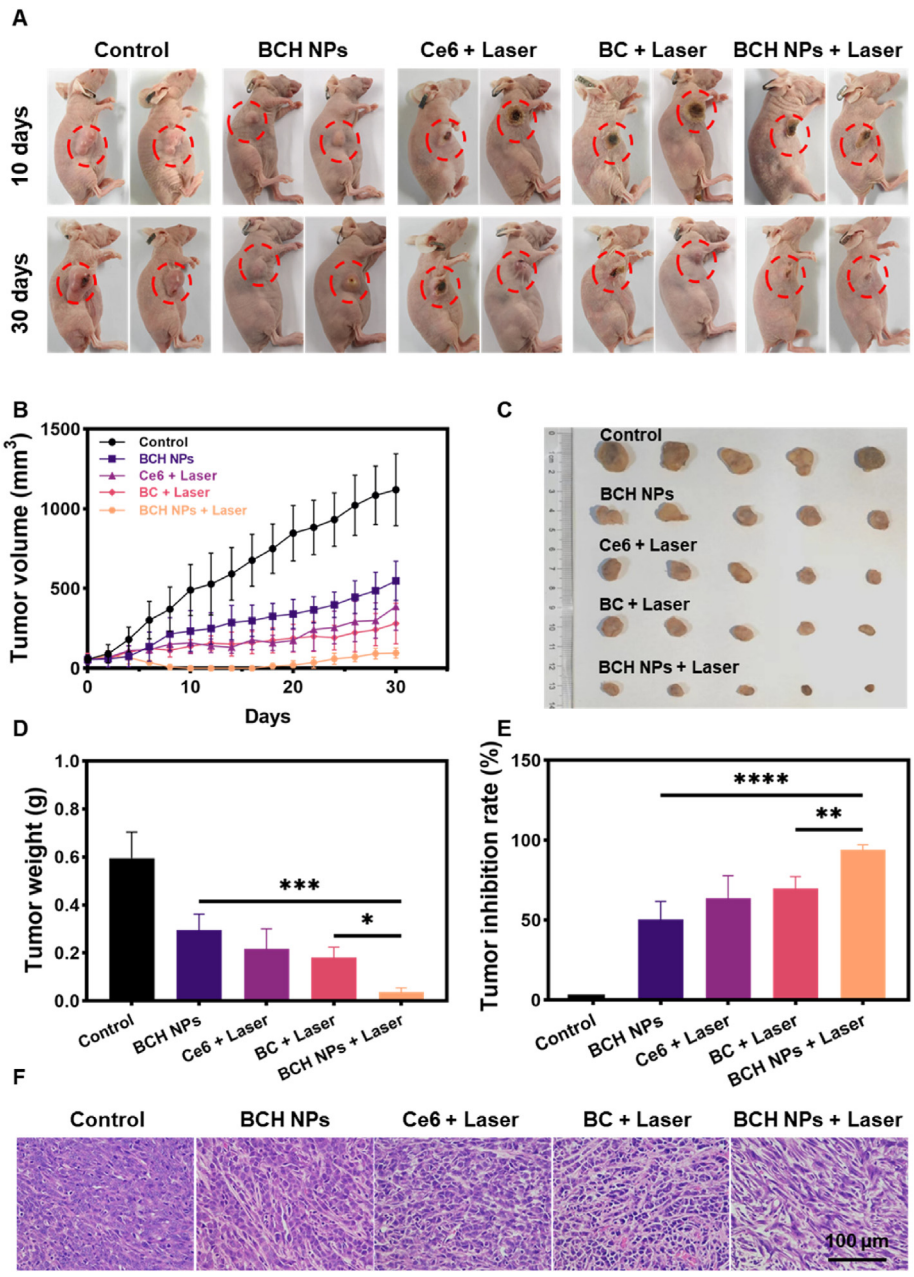

Fig. 4. (A) Representative photos of TNBC-bearing mice from different treatment groups in each time point, the red circles mark the tumor sites. (B) The tumor volume changes of different treatments (n = 5). (C) The isolated tumor photos of different treatment groups (n = 5). (D) The tumor weight of different treatment treatments (n = 5). (E) The tumor inhibition rate of different treatment groups (n = 5). (F) H&E staining images of tumors in different treatment groups, scale bar = 100 μm. Statistical significance was calculated via ordinary one-way ANOVA, $^{*}P < 0.05$, $^{**}P < 0.01$.

effectively verified our hypothesis. Although blocking the glutamine metabolic pathway by GLS inhibitor BPTES (BCH NPs without irradiation) could slightly suppress the growth and metastasis of TNBC, the therapeutic effect of BPTES is limited due to the presence of glucose-dependent metabolic compensatory pathways. In addition, the combination effect of BPTES and Ce6 was also limited due to their instability and poor tumor targeting. The effectiveness of BCH NPs + Laser on inhibiting the growth and metastasis of TNBC was mainly ascribed to the preferential accumulation in tumors, and the coordination of photodynamic-mediated glutamine metabolic intervention.

3.6. *In vivo biosafety evaluation*

After multiple intravenous administrations, there was no significant body weight loss in each treatment group (Fig. S7, Supporting Information). And no obvious biological changes were observed in the H&E staining of major organs in each treatment group (Fig. S8, Supporting Information). Additionally, compared with the control group, the classic blood biochemical indexes, ALT, AST, and CREA did not change significantly (Fig. S9, Supporting Information). These results indicated the favorable biocompatibility of BCH NPs.

4. Conclusion

In summary, we successfully proposed an intelligent photodynamic-mediated glutamine metabolic intervention nanodrug (BCH NPs) for triple negative breast cancer therapy. Taking advantage of the intrinsic merits of BPTES and Ce6, BCH NPs achieved effective harmonization of glutamine metabolic intervention. Specifically, Ce6 bolstered the effects of BPTES by generating excessive ROS to deplete GSH produced by glutamine or glucose metabolic pathways. While BPTES in turn ameliorated ROS resistance and amplified the PDT efficacy of Ce6 by inhibiting

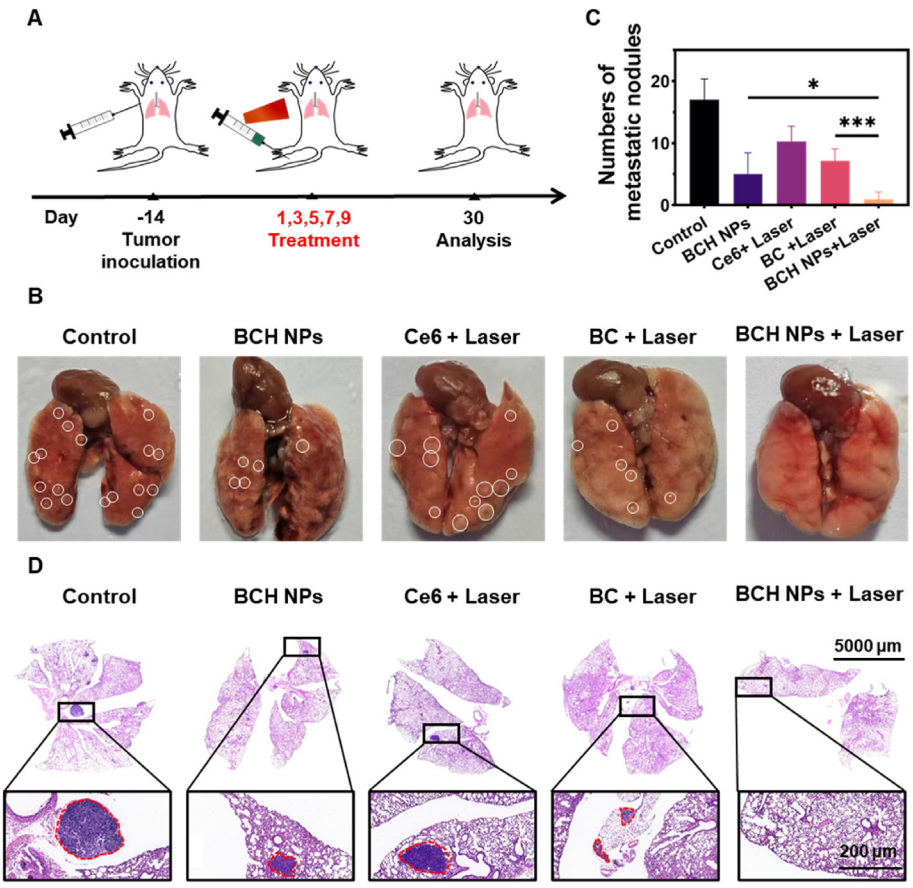

Fig. 5. (A) Experimental design of the anti-metastasis analysis. (B) Representative images of tumor lung metastasis in each treatment group, the white circles refer to lung metastatic nodules. (C) Quantitative results of pulmonary metastatic nodules in each treatment group (n = 8). (D) H&E staining images of lungs in different treatment groups, the red curves represent lung metastasis, scale bar = 5000 μm (above), scale bar = 200 μm (below). Statistical significance was calculated via ordinary one-way ANOVA, $^{*}P < 0.05$, $^{***}P < 0.001$.

GSH. Under light irradiation, BCH NPs treatment effectively eradicated TNBC tumor and suppressed tumor metastasis with favorable biocompatibility. Our work presents a safe and feasible nanodrug for photodynamic-mediated glutamine metabolic intervention and holds great potential for clinical translation of TNBC therapy.

Credit author statement

Cancan Yu: Conceptualization, Methodology, Writing - original draft, Formal analysis, Investigation. **Ningning Wang**: Conceptualization, Methodology, Investigation. **Xiangwu Chen**: Formal analysis, Investigation. **Yue Jiang**: Writing - original draft, Formal analysis, Funding acquisition. **Yuxia Luan**: Formal analysis, Funding acquisition. **Wen Qin**: Writing -review & editing, Supervision. **Wenxiu He**: Writing -review & editing, Supervision, Funding acquisition.

Declaration of competing interest

The authors declare that they have no known competing financial interests or personal relationships that could have appeared to influence the work reported in this paper.

Data availability

Data will be made available on request.

Acknowledgements

We acknowledge the Pharmaceutical Biology Sharing Platform of school of Pharmaceutical Sciences, Cheeloo College of Medicine, Shandong University. This project was financially supported by the National Natural Science Foundation of China (NSFC, No. 82061148009, No. 81903558, No. 21872083, No. 82204305), and Joint Funds of Natural Science Foundation of Shandong Province (ZR202108050005).

Appendix A. Supplementary data

Supplementary data to this article can be found online at https://doi.org/10.1016/j.mtbio.2023.100577.

References

[1] H. Sung, J. Ferlay, R.L. Siegel, M. Laversanne, I. Soerjomataram, A. Jemal, F. Bray, Global cancer statistics 2020: GLOBOCAN estimates of incidence and mortality worldwide for 36 cancers in 185 countries, Ca-Cancer J, Clinic 71 (3) (2021) 209–249.
[2] X.Y. Sun, M.Z. Wang, M.S. Wang, X.T. Yu, J.Y. Guo, T. Sun, X.Y. Li, L.T. Yao, H.R. Dong, Y.Y. Xu, Metabolic reprogramming in triple-negative breast cancer, Front. Oncol. 10 (2020) 428–443.
[3] C. Denkert, C. Liedtke, A. Tutt, G. von Minckwitz, Molecular alterations in triple-negative breast cancer-the road to new treatment strategies, Lancet 389 (10087) (2017) 2430–2442.
[4] V. Gote, A.R. Nookala, P.K. Bolla, D. Pal, Drug resistance in metastatic breast cancer: tumor targeted nanomedicine to the rescue, Int. J. Mol. Sci. 22 (9) (2021) 4673–4713.
[5] M.D. Cao, S. Lamichhane, S. Lundgren, A. Bofin, H. Fjosne, G.F. Giskeodegard, T.F. Bathen, Metabolic characterization of triple negative breast cancer, BMC Cancer 14 (2014) 941–952.
[6] N.N. Pavlova, C.B. Thompson, The emerging hallmarks of cancer metabolism,, Cell Metabol. 23 (1) (2016) 27–47.
[7] U.E. Martinez-Outschoorn, M. Peiris-Pages, R.G. Pestell, F. Sotgia, M.P. Lisanti, Cancer metabolism: a therapeutic perspective, Nat. Rev. Clin. Oncol. 14 (2) (2017) 11–31.
[8] S. Kumari, R.R. Malla, Recent advances in metabolomics of triple negative breast cancer, Breast J. 26 (3) (2020) 498–501.
[9] B.J. Altman, Z.E. Stine, C.V. Dang, From Krebs to clinic: glutamine metabolism to cancer therapy, Nat. Rev. Cancer 16(12) (2016) 619–634.

[10] M.J. Lukey, K.S. Greene, J.W. Erickson, K.F. Wilson, R.A. Cerione, The oncogenic transcription factor c-Jun regulates glutaminase expression and sensitizes cells to glutaminase-targeted therapy, Nat, Commun. Now. 7 (2016) 11321–11325.
[11] M. van Geldermalsen, Q. Wang, R. Nagarajah, A.D. Marshall, A. Thoeng, D. Gao, W. Ritchie, Y. Feng, C.G. Bailey, N. Deng, K. Harvey, J.M. Beith, C.I. Selinger, S.A. O'Toole, J.E. Rasko, J. Holst, ASCT2/SLC1A5 controls glutamine uptake and tumour growth in triple-negative basal-like breast cancer, Oncogene 35 (24) (2016) 3201–3208.
[12] L. Yang, T. Moss, L.S. Mangala, J. Marini, H. Zhao, S. Wahlig, G. Armaiz-Pena, D. Jiang, A. Achreja, J. Win, R. Roopaimoole, C. Rodriguez-Aguayo, I. Mercado-Uribe, G. Lopez-Berestein, J. Liu, T. Tsukamoto, A.K. Sood, P.T. Ram, D. Nagrath, Metabolic shifts toward glutamine regulate tumor growth, invasion and bioenergetics in ovarian cancer, Mol. Syst. Biol. 10 (5) (2014) 728–751.
[13] L. Yang, S. Venneti, D. Nagrath, Glutaminolysis: a hallmark of cancer metabolism, Annu. Rev. Biomed, Eng. Times 19 (2017) 163–194.
[14] X.Y. Li, M. Wenes, P. Romero, S.C.C. Huang, S.M. Fendt, P.C. Ho, Navigating metabolic pathways to enhance antitumour immunity and immunotherapy, Nat. Rev. Clin. Oncol. 16 (7) (2019) 425–441.
[15] Y. Xiang, Z.E. Stine, J.S. Xia, Y.Q. Lu, R.S. O'Connor, B.J. Altman, A.L. Hsieh, A.M. Gouw, A.G. Thomas, P. Gao, L.C. Sun, L.B. Song, B. Yan, B.S. Slusher, J.L. Zhuo, L.L. Ooi, C.G.L. Lee, A. Mancuso, A.S. McCallion, A. Le, M.C. Milone, S. Rayport, D.W. Felsher, C.V. Dang, Targeted inhibition of tumor-specific glutaminase diminishes cell-autonomous tumorigenesis, J. Clin. Invest. 125 (6) (2015) 2293–2306.
[16] A. Le, A.N. Lane, M. Hamaker, S. Bose, A. Gouw, J. Barbi, T. Tsukamoto, C.J. Rojas, B.S. Slusher, H.X. Zhang, L.J. Zimmerman, D.C. Liebler, R.J.C. Slebos, P.K. Lorkiewicz, R.M. Higashi, T.W.M. Fan, C.V. Dang, Glucose-independent glutamine metabolism via tCA cycling for proliferation and survival in B Cells, Cell Metabol. 15 (1) (2012) 110–121.
[17] T.L. Cheng, J. Sudderth, C.D. Yang, A.R. Mullen, E.S. Jin, J.M. Mates, R.J. DeBerardinis, Pyruvate carboxylase is required for glutamine-independent growth of tumor cells, P. Natl. Acad. Sci. USA 108 (21) (2011) 8674–8679.
[18] J.E. Bader, K. Voss, J.C. Rathmell, Targeting metabolism to improve the tumor microenvironment for cancer immunotherapy, Mol. Cell. 78 (6) (2020) 1019–1033.
[19] X.S. Li, J.F. Lovell, J. Yoon, X.Y. Chen, Clinical development and potential of photothermal and photodynamic therapies for cancer, Nat. Rev. Clin. Oncol. 17 (11) (2020) 657–674.
[20] M.H. Lan, S.J. Zhao, W.M. Liu, C.S. Lee, W.J. Zhang, P.F. Wang, Photosensitizers for photodynamic therapy, Adv. Healthc. Mater 8 (13) (2019) 132–168.
[21] Y.X. Xiong, C. Xiao, Z.F. Li, X.L. Yang, Engineering nanomedicine for glutathione depletion-augmented cancer therapy, Chem. Soc. Rev. 50 (10) (2021) 6013–6041.
[22] M. Zhang, X. Qin, Z. Zhao, Q. Du, Q. Li, Y. Jiang, Y. Luan, A self-amplifying nanodrug to manipulate the Janus-faced nature of ferroptosis for tumor therapy,, Nanoscale Horiz 7 (2) (2022) 198–210.
[23] P.Z. Wang, P. Yang, K. Qian, Y.X. Li, S.T. Xu, R. Meng, Q. Guo, Y.L. Cheng, J.X. Cao, M.J. Xu, W. Lu, Q.Z. Zhang, Precise gene delivery systems with detachable albumin shell remodeling dysfunctional microglia by TREM2 for treatment of Alzheimer's disease, Biomaterials 281 (2022) 121360–121376.
[24] Y. Fu, H.H. Han, J. Zhang, X.P. He, B.L. Feringa, H. Tian, Photocontrolled fluorescence "Double-Check" bioimaging enabled by a glycoprobe-protein hybrid, J. Am. Chem. Soc. 140 (28) (2018) 8671–8674.
[25] X.L. Hu, N. Kwon, K.C. Yan, A.C. Sedgwick, G.R. Chen, X.P. He, T.D. James, J. Yoon, Bio-conjugated advanced materials for targeted disease theragnostic, Adv. Funct. Mater. 30 (13) (2020) 1907906–1907930.
[26] J.P. Wei, J.C. Li, D. Sun, Q. Li, J.Y. Ma, X.L. Chen, X. Zhu, N.F. Zheng, A novel theranostic nanoplatform based on Pd@Pt-PEG-Ce6 for enhanced photodynamic therapy by modulating tumor hypoxia microenvironment, Adv. Funct. Mater. 28 (17) (2018) 1706310–1706321.
[27] X. Hu, H. Tian, W. Jiang, A. Song, Z. Li, Y. Luan, Rational design of IR820- and Ce6-based versatile micelle for single NIR laser-induced imaging and dual-modal phototherapy, Small 14 (52) (2018) 1802994–1803005.
[28] L.H. Wu, X.J. Cai, H.F. Zhu, J.H. Li, D.X. Shi, D.F. Su, D. Yue, Z.W. Gu, PDT-Driven highly efficient intracellular delivery and controlled release of CO in combination with sufficient singlet oxygen production for synergistic anticancer therapy, Adv. Funct. Mater. 28 (41) (2018) 1804324–1804336.
[29] H. Cai, P. Tan, X.T. Chen, M. Kopytynski, D.Y. Pan, X.L. Zheng, L. Gu, Q.Y. Gong, X.H. Tian, Z.W. Gu, H. Zhang, R.J. Chen, K. Luo, Stimuli-sensitive linear-dendritic block copolymer-drug prodrug as a nanoplatform for tumor combination therapy, Adv. Mater. 34 (8) (2022) 2108049–2108063.
[30] X.P. Duan, Y.P. Li, Physicochemical characteristics of nanoparticles affect circulation, biodistribution, cellular internalization, trafficking, Small 9 (9-10) (2013) 1521–1532.
[31] C.R. Park, J.H. Jo, M.G. Song, J.Y. Park, Y.H. Kim, H. Youn, S.H. Paek, J.K. Chung, J.M. Jeong, Y.S. Lee, K.W. Kang, Secreted protein acidic and rich in cysteine mediates active targeting of human serum albumin in U87MG xenograft mouse models, Theranostics 9 (24) (2019) 7447–7457.
[32] N. Desai, V. Trieu, B. Damascelli, P. Soon-Shiong, SPARC expression correlates with tumor response to albumin-bound paclitaxel in head and neck cancer patients, Transl. Oncol 2 (2) (2009) 59–64.
[33] K. Greish, Enhanced permeability and retention (EPR) effect for anticancer nanomedicine drug targeting, Methods Mol. Biol. 624 (2010) 25–37.
[34] F. Kratz, Albumin as a drug carrier: design of prodrugs, drug conjugates and nanoparticles, J. Control Release 132 (3) (2008) 171–183.
[35] X. Chai, H.H. Han, A.C. Sedgwick, N. Li, Y. Zang, T.D. James, J. Zhang, X.L. Hu, Y. Yu, Y. Li, Y. Wang, J. Li, X.P. He, H. Tian, Photochromic fluorescent probe strategy for the super-resolution imaging of biologically important biomarkers, J. Am. Chem. Soc. 142 (42) (2020) 18005–18013.
[36] Z. Luo, J. Xu, J. Sun, H. Huang, Z. Zhang, W. Ma, Z. Wan, Y. Liu, A. Pardeshi, S. Li, Co-delivery of 2-Deoxyglucose and a glutamine metabolism inhibitor V9302 via a prodrug micellar formulation for synergistic targeting of metabolism in cancer, Acta Biomater. 105 (2020) 239–252.
[37] R.D. Leone, L. Zhao, J.M. Englert, I.M. Sun, M.H. Oh, I.H. Sun, M.L. Arwood, I.A. Bettencourt, C.H. Patel, J. Wen, A. Tam, R.L. Blosser, E. Prchalova, J. Alt, R. Rais, B.S. Slusher, J.D. Powell, Glutamine blockade induces divergent metabolic programs to overcome tumor immune evasion, Science 366 (6468) (2019) 1013–1021.
[38] C.T. Hensley, A.T. Wasti, R.J. DeBerardinis, Glutamine and cancer: cell biology, physiology, and clinical opportunities, J. Clin. Invest. 123 (9) (2013) 3678–3684.
[39] W.T. Dou, H.H. Han, A.C. Sedgwick, G.B. Zhu, Y. Zang, X.R. Yang, J. Yoon, T.D. James, J. Li, X.P. He, in: Fluorescent Probes for the Detection of Disease-Associated Biomarkers, vol. 67, Sci. Bull., Beijing, 2022, pp. 853–878 (8).
[40] D.R. Sappington, E.R. Siegel, G. Hiatt, A. Desai, R.B. Penney, A. Jamshidi-Parsian, R.J. Griffin, G. Boysen, Glutamine drives glutathione synthesis and contributes to radiation sensitivity of A549 and H460 lung cancer cell lines, Biochim. Biophys, Acta 1860(4) (2016) 836–843.
[41] A. Le, A.N. Lane, M. Hamaker, S. Bose, A. Gouw, J. Barbi, T. Tsukamoto, C.J. Rojas, B.S. Slusher, H. Zhang, L.J. Zimmerman, D.C. Liebler, R.J. Slebos, P.K. Lorkiewicz, R.M. Higashi, T.W. Fan, C.V. Dang, Glucose-independent glutamine metabolism via TCA cycling for proliferation and survival in B cells, Cell Metabol. 15 (1) (2012) 110–121.
[42] M. Zhang, X. Qin, Z. Zhao, Q. Du, Q. Li, Y. Jiang, Y. Luan, A self-amplifying nanodrug to manipulate the Janus-faced nature of ferroptosis for tumor therapy,, Nanoscale Horiz 7 (2) (2022) 198–210.
[43] M. Belicza, Evaluation of morphologically determined apoptotic index, Acta Med, Croatica 63 (Suppl 2) (2009) 3–12.